

Spray flame structure in conventional and hot-diluted combustion regime

Hugo Correia Rodrigues, Mark J. Tummers, Eric H. van Veen, Dirk J.E.M. Roekaerts *

Department of Process and Energy, Section Fluid Mechanics, Delft University of Technology, Mekelweg 2, 2628 CD Delft, The Netherlands



ARTICLE INFO

Article history:

Received 3 February 2014

Received in revised form 7 May 2014

Accepted 7 July 2014

Available online 9 September 2014

Keywords:

Spray flames

MILD combustion

Liquid breakup

Hot-diluted coflow

PDA

CARS

ABSTRACT

A laboratory scale experimental setup was built to study ethanol pressure-swirl spray flames in a coflow of either air or hot-diluted oxidant. The latter case resembles conditions similar to those found in practical combustion systems of liquid fuels operating in MILD conditions.

First, experiments have been performed to investigate the phenomena associated with the atomization process. High-speed visualizations show that in the presence of a hot-diluted coflow, an almost immediate disruption of the liquid jet takes place, indicating significant changes in the atomization mechanism, compared to the case with air coflow. Secondly, a comprehensive set of measurements was obtained by complementary single-point measurement techniques to reveal the gas and droplets flow fields as well as temperature fields. Measurements of droplet size and velocity components in the spray region were obtained by phase Doppler anemometry. Gas temperature was measured using coherent anti-Stokes Raman spectroscopy even in regions with droplet density as high as 10^5 cm^{-3} . It has been observed that in a reacting spray in air coflow, an inner and an outer flame-front are present. For a reacting spray with similar injection pressure in hot-diluted coflow, weakening of the inner flame-front is attributed to the fact that the gaseous mixture becomes increasingly rich towards the center region. Consequently, a significant reduction of occurrence of temperature samples above 2000 K is observed throughout most of the spray region.

© 2014 The Combustion Institute. Published by Elsevier Inc. All rights reserved.

1. Introduction

The technology of Moderate and Intense Low oxygen Dilution combustion, or 'flameless combustion' relies on the dilution of fresh reactants with cooled recirculated combustion products prior to the main combustion zone thereby lowering flame adiabatic temperature and, consequently, reducing significantly nitric oxides (NO_x) emissions [1]. For this process to be effective, a combination of sufficiently large recycle ratio of combustion products and a mixture temperature exceeding the auto-ignition temperature of the fuel is required [2–4].

The most notable and comprehensive experimental studies on MILD conditions were performed in laboratory scale non-premixed gaseous flames. Those studies consist of symmetric jet flames issuing into a stable hot and diluted coflow. Dally et al. [5] developed a jet-in-hot-coflow (JHC) burner able to operate at a wide range of coflow temperatures and O_2 levels. In the reported experiments the oxygen mass percentage in the oxidizer coflow ranged from 3% to 9%. Measurements of reactive scalars in a CH_4/H_2 flame were

performed only at one side of the flame. Modeling studies of these flames revealed that the accurate representation of the initial coflow radial profiles of velocity statistics and scalar statistics are of utmost importance [6]. Oldenhoef et al. [7,8] constructed a similar JHC burner, but modified the secondary burner to allow optical measurement techniques for flow velocity based on tracer particles. Mean velocity and temperature fields were measured in non-premixed Dutch natural gas flames in a hot coflow with oxygen mass percentage ranging from 7.6% to 10.9% [7]. A small temperature increase was found in the shear region and, velocity and turbulent stresses profiles in the reaction zones were not significantly affected by the chemical reactions [7]. High-speed recordings of the luminescence at the flame base, showed that the stabilization mechanism is based on auto-ignition kernels that grow into large pockets [8].

Compared to turbulent gaseous flames, in turbulent spray flames additional phenomena come into play. Mixing of a disintegrating liquid jet with its surroundings differs from that of a gaseous jet. To create the spray flame, the fuel stream first has to be disintegrated into an ensemble of droplets with a desirable distribution of sizes and velocities in order to achieve the required rate of vaporization, chemical heat-release, levels of conversion and

* Corresponding author. Fax: +31 15 27 82838

E-mail address: D.J.E.M.Roekaerts@tudelft.nl (D.J.E.M. Roekaerts).

pollutant emissions. Instabilities at the liquid–gas interface in the near-atomizer region lead to primary and secondary break-up. The liquid fragments in surrounding gas form a dispersed multi-phase flow, where droplets are evaporating and subject to turbulent dispersion. The dispersed droplets modify the gas-phase turbulence and the released fuel vapor depending on the relative speed of evaporation, mixing and combustion, burns in diffusion flames around individual droplets or clusters of droplets, or in partially premixed gaseous flames [9]. Also the temperature and composition of the oxidizer influences the time scales of phase change and reaction, making a spray flame in hot-diluted combustion regime different from that of a conventional spray flame in air.

The viability of combustion of liquid fuel in a diluted oxidizer at industrial and semi-industrial scale has been investigated in the literature. Tsuji et al. [10] reported experiments in a kerosene spray flame oxidized by preheated air diluted with combustion products with an oxygen percentage ranging from 3% to 10%. Weber et al. [11] performed experiments on MILD combustion of light fuel oil in a furnace at a power of 0.58 MW. Recently, Reddy et al. [12,13] reported experimental and numerical studies of a two-stage labscale combustor where MILD conditions were reached using intense swirl. These investigations provide encouraging results on the applicability of MILD combustion to liquid fuels. However, the configurations studied did not allow for detailed laser diagnostic measurements needed to obtain insights on the fundamental aspects of this combustion technique.

The present work concerns an experimental study. The objective is to reach understanding, in an analogous way as done for gaseous fuels, by using a special burner design allowing for detailed observations. A laboratory scale burner was developed to study spray combustion under MILD conditions. The burner design retains the relevant physical processes of practical combustion systems. However, the composition of the gases entrained into the spray are controlled by a secondary burner rather than the furnace aerodynamics. Moreover, the spray flame is unconfined, allowing good optical access for complementary laser diagnostic techniques. Ethanol was used as fuel because of the well-defined properties. Fuel atomization is done using a commercial pressure-swirl atomizer. To clearly identify the characteristics of MILD combustion in comparison to conventional combustion two cases are considered. In the first case the fuel jet is injected in a coflow of ambient air and in the second case in a hot-diluted coflow with 9.2% oxygen by volume. This study contributes to the current literature in three ways: (a) by advancing the use of laser diagnostic techniques in turbulent spray flames. This is done by reporting, to the authors' knowledge, for the first time gas-phase temperature statistics in the spray region by means of coherent anti-Stokes Raman spectroscopy technique; (b) by providing a comprehensive set of measurements that can be further used as valuable database for model validation of polydispersed sprays [9]; and (c) by providing understanding of the qualitative features of the transition of a liquid jet into a mixture of vapor and stable droplets in a hot surrounding environment.

It is known that the liquid atomization process and the near-atomizer region plays a keyrole in the entire spray flame characteristics and dynamics also further downstream [14,15]. Advanced diagnostic techniques in two-phase flows have been introduced at a slower pace than the gaseous counterparts and it has been difficult to obtain sufficiently accurate experimental data in near field of spray flames. To circumvent this problem, fundamental studies of turbulent spray flames have been made using a nebuliser instead of a pressure atomizer. In this configuration, the complexity induced by the near-atomizer effects in the dense-region of a pressure atomizer can be avoided and dilute spray flames with simple and well-defined boundary conditions studied. Karpetis and Gomez [16] reported on a series of experiments using methanol fuel. O'Loughlin and Masri [17] extended the burner design of Karpetis

and Gomez to study the effect of a hot-diluted coflow on a dilute spray. Simultaneous high-speed OH–CH* Planar LIF and droplet Mie scattering show that ignition OH kernels formation and growth is the mechanism of spray flame stabilization in hot-diluted conditions. It may be argued though that the oxygen mole fraction in the coflow (12% by volume) is rather high compared to other studies of combustion systems operating in MILD conditions [10,18].

In the present study a commercial atomizer was used for generating the spray instead of a nebulizer, because we considered it important to remain close to the most common configuration used in industrial practice. The results provide a valuable dataset for model validation of sprays in MILD conditions and complements other datasets already available in the literature [9]. The model validation studies conducted on other experimental databases [19–22], have used a variety of RANS based approaches, as reviewed by Jenny et al. [9]. It is observed that the selection of more advanced submodels for turbulence-chemistry interaction yield better predictions, e.g. progressing from flamelet model to spray flamelet model, or from assumed PDF to transported PDF. Sensitivity to inlet boundary conditions and difficulty to predict correct spreading of the spray and mean temperature have been reported in several of the modeling studies. The literature review also shows successful modeling studies using Large Eddy Simulation (LES) for several types of spray flames burning outside the MILD combustion regime. For example, a swirl stabilized kerosene flame was studied using LES-PDF with stochastic field method by Jones et al. [23]. A pilot-stabilized ethanol flame was studied using LES-PDF with stochastic particle method by Heyes et al. [24] and using LES-CMC by Ukai et al. [25]. The studies show that in LES sufficient precision in the representation of the turbulence-chemistry interaction on the subgrid scale is necessary.

In view of this, complementary pointwise laser-based measurement techniques were employed separately in the coflow inlet conditions and spray region to obtain a detailed and accurate dataset for model validation. The presented dataset is sufficiently complete to eliminate or at least constrain possibilities to get good model predictions by merely tuning of model constants. All measurements are made up to locations as close to the atomizer as possible. Additionally, high-speed visualizations were carried out to unveil the atomization mechanisms of the different spray flames. The use of new experimental techniques such as ballistic imaging [26] and X-ray absorption methods [27], would enable further progress towards a more complete measurements. Also detailed numerical studies [28] have the potential to provide understanding and detailed description of the atomization process. These advanced experimental and numerical techniques could be used to complement the observations using high speed camera reported here.

This paper is structured as follows: Section 2 briefly describes the burner facility and measurement techniques used in the present study. Section 3 presents the input parameters for three test-cases: non-reacting evaporating spray, reacting spray in air coflow and reacting spray in hot-diluted coflow. Section 4 presents results on: (1) Comprehensive description of the coflow inlet turbulent characteristics; (2) high-speed visualization and analysis of liquid jet breakup and, last, (3) a discussion of the most notable features of spray flames structure in air and hot-diluted coflow. In Section 6, conclusions are presented.

2. Experimental method

2.1. Burner facility

Figure 1 shows a schematic of the burner facility. It consists of a pressure-swirl atomizer that produces a spray of fine fuel droplets issuing in a coflow of either air or hot combustion products.

Hereafter, these two cases will be referred to as 'air coflow' and 'hot-diluted coflow' respectively.

The hot-diluted coflow is produced by the secondary burner that operates on air and Dutch natural gas (DNG) to generate a matrix of 236 lean flamelets. The typical molar composition of DNG is 81.3% methane, 14.4% nitrogen, 3.7% ethane and 0.6% of other species. A vertical pipe with 270 mm length and 160 mm inner diameter prevents the coflow from mixing with the surrounding air. Moreover, it also establishes an enthalpy deficit by radiation to the environment reducing the temperature of the hot combustion products. The two perforated plates installed in the vertical pipe keep the central fuel rod concentric and also contribute to the coflow enthalpy loss through radiation. The air-to-DNG ratio together with the effects of the two perforated plates and the pipe length dictate the coflow temperature, oxygen concentration and turbulence levels. The mass flow rates for air and DNG were set by Bronkhorst mass flow controllers with an inaccuracy of $\pm 0.5\%$ of the full scale.

Above a certain axial location the effects of the entrainment of the surrounding air into the hot-diluted coflow have substantial effects on the flame structure [29,30]. These flames are essentially a three-stream mixing problem, i.e. fuel jet, hot-diluted coflow and surrounding air, increasing to a great extent data interpretation and analysis as well as the complexity of numerical simulations [6,31]. Hence, the coflow diameter was chosen large enough to isolate the spray flame from the surrounding laboratory air as much as possible.

The spray was produced by a commercial pressure-swirl solid cone atomizer (Delavan WDA 0.5 GPH) with an 0.21 mm exit orifice and a 60° spray angle mounted on a 2 mm inner diameter stainless steel pipe through which liquid fuel is fed to the atomizer. The liquid fuel used in the present study is ethanol (C_2H_5OH). To prevent excessive heating and possible pre-vaporization of the ethanol, the fuel pipe is water-cooled and several layers of thin stainless steel foils are wrapped around the cooled fuel pipe to form a

radiation heat shield. Liquid fuel temperature is monitored at the atomizer inlet by means of a type K thermocouple (Thermocoax). The liquid fuel pressure is measured with a pressure transducer (Omegadyne MMA). The analog output of the pressure transducer is fed to the external data collection system of a TSI PDA system for simultaneous measurement of pressure and droplet size and velocity. Liquid flow rates were set by a Bronkhorst mini-Coriolis mass flow controller with $\pm 0.2\%$ inaccuracy. The burner can move in three orthogonal directions by means of a traversing system equipped with computer-controlled stepping motors. Throughout this paper, a r , z -coordinate system is used with its origin at the atomizer orifice exit plane. The z -coordinate is measured along the axis of the burner and r denotes the radial coordinate.

2.2. Measurement techniques

In this study, five measurements techniques were separately employed: laser Doppler anemometry, phase Doppler anemometry, coherent anti-Stokes Raman spectroscopy, high-speed visualization and flue gas analyser. A brief description of each system used is given below.

2.2.1. Laser Doppler Anemometry (LDA)

LDA measurements were performed at $z = 0$ mm, i.e. at the atomizer orifice exit plane and, also, on one test case where no droplets are present along the spray axis. The results provide the input boundary conditions needed for numerical simulations as well as relevant information to understand of the spray flame behavior. The LDA consists of a two-component, dual beam TSI-system operating in back-scattering mode. The green line (514.5 nm) and blue line (488 nm) of a 10 W Continuum Argon-ion laser were used to measure axial and radial velocity components (U_z and U_r , respectively). The transmitting optics had a focal length of 350 mm and yielded a measurement volume of 0.17 mm in diameter and 2.40 mm in length. The photomultiplier output signals were fed to a TSI FSA-3000 processor. Aluminum oxide particles (Al_2O_3) with an average diameter of 1 μm were added to the air by using a cyclone seeder. At each measurement position 10^4 samples were acquired to ensure adequate convergence of the second-order moments. Velocity statistics were computed using the transit time as a weighting factor to compensate for the velocity bias [32]. Consequently, the velocity statistics should be interpreted as Favre-averaged quantities [7]. According to the results of the detailed analysis of the various error sources in LDA measurements as reported by Absil [33] we assume that the mean velocity components are accurate up to 2% of the maximum flow velocity. The Reynolds normal stresses and the Reynolds shear stress are accurate up to 5% and 8% of their local maximum values, respectively.

2.2.2. Phase Doppler Anemometry (PDA)

PDA measurements provided simultaneous droplet velocity and size statistics in the spray region. The transmitting optics used for the PDA are identical to those of the LDA system. The receiving optics were set up to collect mainly first-order refracted light ($p = 1$). The front and internal lenses had focal lengths of 650 mm and 250 mm, respectively and imaged the measurement volume onto a 150 μm slit. The signal processing was performed by a TSI FSA-4000 processor and the associated FlowSizer software. At each measurement point 3×10^4 samples were acquired except at those points with data rates less than 100 Hz where 10^4 samples were taken.

Velocity and size statistics of a ensemble of droplets can be significantly affected by adjustable parameters of the PDA measurement system [32]. To ensure accurate measurement results, a parametric study was performed prior to the experimental

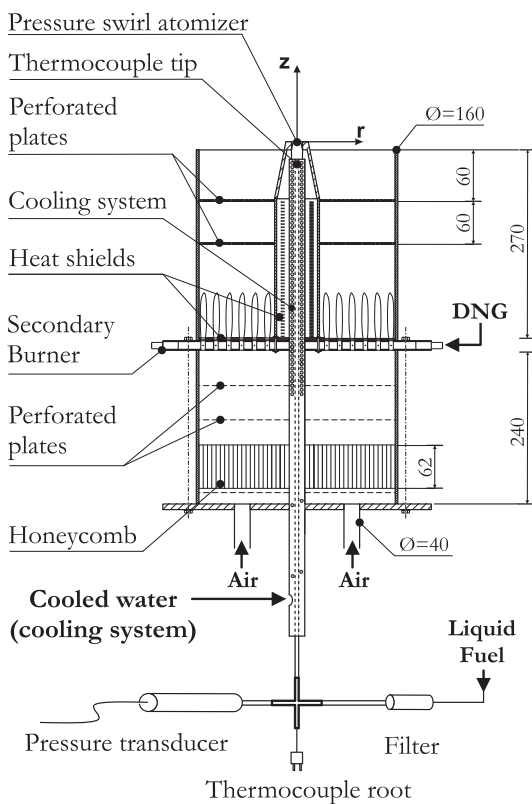


Fig. 1. Schematic of the burner facility with relevant dimensions in millimeters.

campaign. All the parameters of the PDA system as well as those of the Argon-ion laser, were kept constant throughout the measurement campaign. An intensity validation scheme in the software was used to reject occurrences with multiple droplets in the probe volume and large droplets that are erroneously sized as small. The parameters of the intensity validation scheme were determined in a very dilute-region of the spray flame where the condition that there is only one particle at a time in the measurement volume is fulfilled.

Care was taken to account for the Gaussian light intensity distribution in the measurement volume on the sizing measurements. Larger droplets scatter more light and therefore can be detected farther away from the center of the probe volume than smaller droplets. A probe volume correction based on the maximum path length for each particle size class was used to correct representative droplet diameter statistics bias [34]. An other aspect is that, for small droplets, more than one dominant mode of scattered light may be present depending on the droplet trajectory. This results in the droplets being erroneously sized. In order to avoid bias on the gas-phase statistics, only droplets with a $\pm 1 \mu\text{m}$ tolerance between the phase difference of the three detectors were considered from the full record [35].

Gas-phase velocity statistics were derived by selecting from the full record droplets that were suitable tracers of the continuous phase. The small droplets generated at the breakup can better follow the flow field because of the relatively small inertia. The larger droplets, ejected from the liquid jet at relatively high velocity, at first maintain their initial velocity because of inertia effects. This implies that, the inclusion of large droplets as flow tracers potentially bias the gas-phase velocity statistics. Velocity statistics were estimated for several droplet threshold sizes. The upper size limit of droplets below which no major differences of the velocity statistics are observed was selected.

Based on the work of Widmann and Presser [21], the inaccuracy associated with the droplet mean velocity is about 4%. Oscillations in the PDA response are found to occur for small droplets and results in different sizing error depending on the droplet diameter. According to the work of Taylor et al. [36], sizing errors for droplets below $1 \mu\text{m}$ are on the order of 60%. Above $1 \mu\text{m}$, the sizing errors are approximately 8%. For further details on PDA errors and uncertainties we refer to the work of Friedmann and Renksizbulut [37].

The droplet diameter is estimated based on the phase shift between the Doppler signals and the droplet refractive index. In a reacting spray, the temperature increase of the droplet and its surrounding gaseous phase results in a reduction of the relative refractive index. Thus, the PDA measurement is susceptible to droplet diameter bias if the properties of the droplet are not measured simultaneously. In the spray flame in air coflow, at the lift-off height axial position, the refractive index ranges from 1.365 to 1.333 over the temperature range from 20 °C to near boiling at 78.1 °C. This results in a systematic error up to 3% in the droplet diameter. More downstream in the spray where droplets are close to boiling, the effect of temperature on the refractive index of ethanol is negligible. For the spray flame in hot-diluted case, an estimation of the droplet temperature at the first measurement station indicates that droplets are at boiling temperature. Thus, this effect does not occur.

2.2.3. Coherent Anti-Stokes Raman Spectroscopy (CARS)

The CARS system was employed to evaluate the gas-phase temperature statistics at $z = 0 \text{ mm}$ and in the spray region. A brief description of the CARS system and data post-processing procedure is reported here but for further details the reader is referred to van Veen and Roekaerts [38,39]. The rovibrational CARS system is based on an injection-seeded, frequency-doubled Nd:YAG laser (Spectron SL805 SLM). Its second harmonic at 532 nm has a

maximum pulse energy of 520 mJ at a 10 Hz repetition rate. About 80% of the radiation is used to pump a modeless Stokes dye laser (Mode-X ML-3), emitting a broadband profile around 607 nm by using Rhodamine 640 in methanol. The remaining 20% of the pump laser radiation travels along a delay line and is then split into two beams with equal intensity. The Stokes beam and the two beams at 532 nm are focused by an aplanat lens with a focal length of 300 mm in a planar-boxcars phase-matching configuration. With this configuration, a probe volume of 700 μm length and 35 μm diameter is created. The generated CARS radiation is recollimated and the beam is focused onto the entrance of an echelle spectrometer. The spectrum is dispersed on a CCD detector with 1100×330 pixels and digitized by an 18-bit AD converter and, ultimately, stored.

The CARS spectra are evaluated with the DACAPO-CARS software [40]. The post-processing method includes the steps of: (1) background subtraction, (2) reference of the CARS spectrum to the Stokes excitation profile, and (3) fitting the resulting spectra to a library of theoretical, temperature-dependent spectra. Previous experiments obtained in a burner stabilized adiabatic flame show that the single shot imprecision of the system is 1% at flame temperature and 4% at ambient temperature. The inaccuracy is estimated to be 20 K.

The application of CARS in reacting flows containing droplets, fuel-rich regions and large temperature gradients requires special considerations because of different types of interaction at the probe volume. One challenge for CARS temperature measurements in spray combustion is the droplet-induced dielectric breakdown in regions where large numbers of fuel droplets are present. Two situations can be distinguished depending on the relative position of the droplet with respect to the probe volume. When a droplet in the probe volume is illuminated by the laser radiation, a dielectric breakdown is observed that disrupts or obscures the resonant N_2 -CARS signal. As a consequence, no valid CARS temperature measurement is obtained. In the event of a droplet along the laser beam paths, an incidental increase on the background occurs. The increase consists of a sloping signal, sometimes accompanied with broad structures. Usually, a linear spectral background profile could be evaluated by interpolation between values found at the left- and right-hand sides of the N_2 spectrum. In the regions with high droplet density, 2000 instead of 1000 single-shot spectra were taken to obtain sufficient valid gas temperature measurements without degrading imprecision and inaccuracy. In addition to resonant N_2 signals, nonresonant signals were observed in regions of the sprays. Based on the species present, only ethanol – having a large nonresonant susceptibility – can account for this signal. A quantitative analysis is not possible, but by the mere presence of nonresonant signals regions with fuel vapor can be identified qualitatively. Last, in the presence of steep temperature gradients within the CARS probe volume, a substantially lower temperature than the mean temperature will be calculated due to the density effect. The optics focal length and beam distances were selected to reduce the probe volume dimensions and maximize the spatial resolution of the CARS system. Measurements in regions with steep temperature gradients were corrected based on a weighted fit according to the procedure suggested by van Veen and Roekaerts [39].

2.2.4. High-speed visualization

The liquid jet breakup was recorded by using an imaging system consisting of a light source and a high-speed camera. To back-light the liquid jet a powerful LED light (Waldmann – MCXFL 3S) was set on-axis with the camera lens. Images of the liquid breakup region were captured using a Photron Fastcam SA1 camera. A lens bellow (Nikon PB-6) was coupled to the camera

allowing the lens (Micro-Nikkor AF 200 mm) to be moved relative to the chip plane and, hence, reduce the field of view.

2.2.5. Flue gas analyser

A Testo 335 fluegas analyser with a specified inaccuracy of $\pm 0.20\%$ was employed at $z = 0$ mm to measure oxygen volume fraction distribution.

3. Case description

Table 1 summarizes the characteristics of the three different cases (NA_I , A_{II} and H_{II}) that were considered in this study. Case NA_I corresponds to a non-reacting spray in air coflow and was included to elucidate the different features of the liquid sheet breakup by means of a high-speed visualization. Case A_{II} refers to a reacting spray in air coflow whereas H_{II} refers to a reacting spray in hot-diluted coflow. Detailed measurements were carried out only for cases A_{II} and H_{II} and a summary of the experimental techniques and measurements locations are presented in **Table 2**. Results of other cases with different degree of coflow dilution will be reported elsewhere. The data rates of the PDA system can be as high as 15 KHz in the near atomizer region and decrease farther downstream. However, the CARS system operates at a repetition rate of 10 Hz. In view of this, CARS was employed only at certain axial stations since otherwise the data collection time became excessively large.

The quantities p and T_F represent the measured ethanol pressure and temperature, respectively. U_{cf} , T_{cf} and $\langle X_{O_2} \rangle$ represent the coflow bulk velocity, temperature and oxygen volume fraction. For A_{II} and H_{II} , these quantities were obtained by integrating the measured profiles over the cross sectional area of the coflow inlet ($z = 0$ mm). For case NA_I , the coflow bulk velocity is determined from the measured air mass flow rate. The Weber number (We) is defined as $\rho_g U_j^2 l / \sigma$. l is the characteristic liquid film thickness (l) and it was assumed as equal to the nozzle diameter, i.e. 210 μm . U_j represents the difference between the estimated liquid jet velocity from the liquid mass flow rate and the coflow bulk velocity.

The main focus of the paper is on the comparison between the cases A_{II} and H_{II} . In case H_{II} significant heat transfer towards the central rod takes place thereby slightly increasing the liquid fuel temperature and, consequently, changing both viscosity and surface tension. This manifests itself as an increase of the injection pressure for the same liquid mass flow rate as compared to the corresponding air coflow case. Since a decrease of the liquid injection pressure is observed to lead to a loss of symmetry of the spray flame, it was decided to study only spray flames with high injection pressure. The reduction in liquid mass flow rate from case A_{II} to H_{II} is about 14%.

Table 1
Spray and coflow input parameters for the studied test cases.

		Test cases		
		NA_I	A_{II}	H_{II}
\dot{m}_F	[kg/h]	0.70	1.70	1.46
p	[bar]	5.1	12.3	11.5
T_F	[K]	293	296	301
We	[–]	0.46	3.26	0.46
\dot{m}_{air}	[kg/h]	70	20	51
\dot{m}_{DNG}	[kg/h]	–	–	2.13
U_{cf}	[m/s]	0.820	0.245	2.243
T_{cf}	[K]	293	293	1300
$\langle X_{O_2} \rangle$	[%]	21	21	9.2

4. Results and discussion

4.1. Visual appearance of the spray flames

To show the overall flame appearance, color photos of the spray flames for cases A_{II} and H_{II} are shown in **Fig. 2**. The right inset shows a close-up of the spray region and initial development of the flame. The field-of-view measures $220 \times 170 \text{ mm}^2$ (width \times height) and is the same in both cases. The photos were acquired with the same camera settings. In both cases, the atomizer yields a conical spray flame having an enlarging diameter downstream. The images show that flame A_{II} has a stronger luminescence and is shorter than H_{II} .

Three regions can be distinguished in the spray region of the reacting spray in air coflow case (A_{II}) from its visual appearance: a jet liquid breakup region with no apparent presence of reaction, a bluish reaction zone and a sooty yellow zone far downstream. Lift-off height is defined here as the axial distance from the atomizer orifice exit plane, $z = 0$ mm, to the lowest axial position of the bluish reaction zone. Above the lift-off location, two flame-fronts develop from the flame base, one on the coflow side and another inside the spray. Such structure has been previously observed in methanol spray flames surrounded by an annular air duct [41,42]. Three regions can also be distinguished in the spray region based on visual appearance for the reacting spray in hot-diluted coflow (H_{II}): a jet liquid breakup region, a faint bluish reaction zone and faint yellowish zone farther downstream. However, compared to case A_{II} , the flame is weakly luminescent, more transparent and relatively bright in the outer-regions of the spray.

4.2. Coflow details

LDA, CARS and flue gas analyzer were separately used to provide information on velocity, temperature and oxygen volume fraction at the coflow inlet ($z = 0$ mm). The mean axial velocity $\langle U_z \rangle$ and turbulence intensity $u'_z / \langle U_z \rangle$ are plotted in **Fig. 3** for case A_{II} . **Figure 3** also shows the results of additional measurements for a situation without fuel supply to the atomizer to illustrate the effect of the spray on the coflow inlet conditions. The coflow mean axial velocity $\langle U_z \rangle$ and the turbulence intensity $u'_z / \langle U_z \rangle$ for case H_{II} are presented in **Fig. 4**. Information on the coflow mean temperature $\langle T \rangle$, r.m.s. temperature fluctuations T' and oxygen volume fraction $\langle X_{O_2} \rangle$ is presented in **Fig. 5**. A summary of the turbulence statistics and derived quantities at two radial positions in the coflow is given in **Table 3** for cases A_{II} , H_{II} and in the case of an air coflow without the spray. The degree of anisotropy of the coflow is characterized by the ratio between the root-mean-square values of the axial and radial velocity fluctuations u'_z / u'_r .

The Taylor microscale λ_g was determined from autocorrelation functions constructed from time series of the axial velocity component with 2.5×10^5 samples by using the slotting method with local normalization. The locally scaled version of the slotted autocorrelation function is given by [43]:

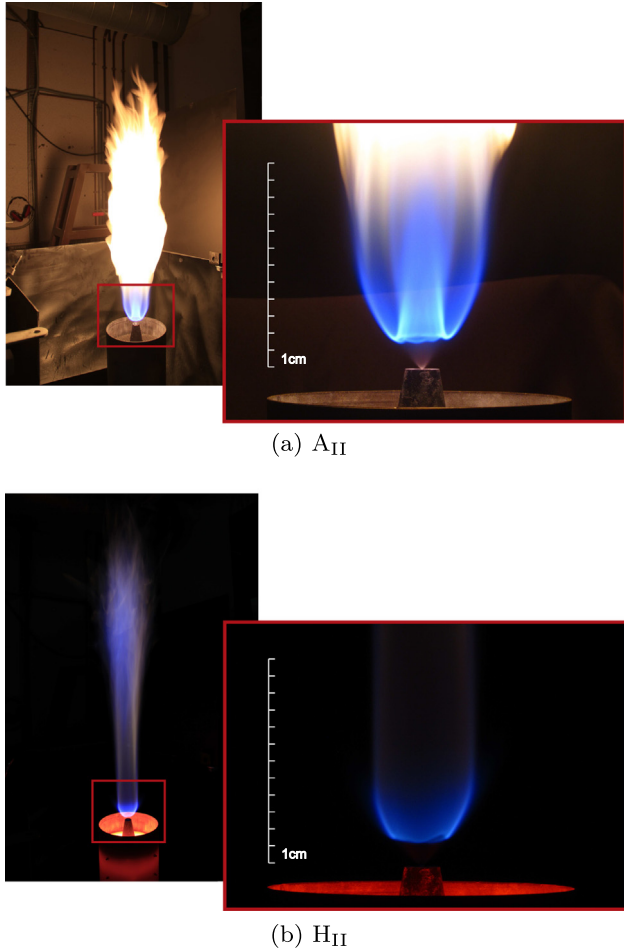
$$\tilde{\rho}(k\Delta\tau) = \frac{\sum \{u_i u_j \omega_i \omega_j(k\Delta\tau)\}}{\sqrt{\sum \{u_i^2 \omega_i \omega_j(k\Delta\tau)\} \sum \{u_j^2 \omega_i \omega_j(k\Delta\tau)\}}} \quad (1)$$

with $k = 0, 1, \dots, M - 1$

where $\{u_i u_j\}(k\Delta\tau)$ denotes the sum of all velocity products $u_i(t_i)u_j(t_j)$ with lag times in the interval $((k - 1/2)\Delta\tau < t_j - t_i < (k + 1/2)\Delta\tau)$. The slot width $\Delta\tau$ is determined from $\Delta\tau = \tau_m / (M - 1)$, where M is the number of slots and τ_m is the maximum lag time. The autocorrelation was corrected for the effects of velocity bias by weighting each cross-product $u_i u_j$ with the corresponding transit times of the particles $\omega_i \omega_j$.

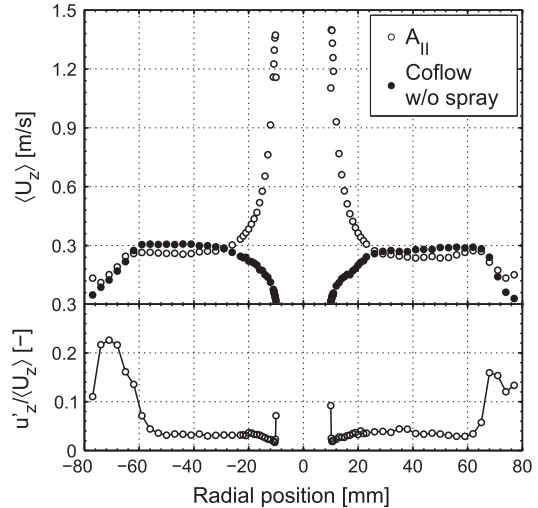
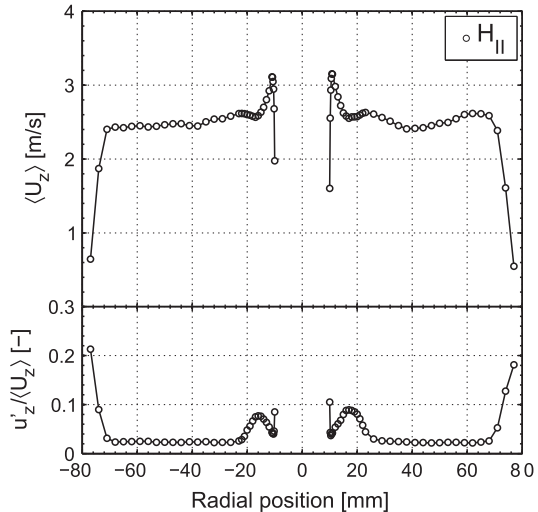
Table 2Summary of measurements locations for A_{II} and H_{II} test cases.

Measurement technique	z (mm)	Comment
LDA	0, 20, 25, 30, 35, 40, 45, 50	Coflow radial profiles, spray center axis
CARS	0, 15, 20, 30, 40, 45, 50, 60	Coflow radial profiles, spray region
Flue gas analyser	0	Coflow radial profiles
PDA	8, 10, 12, 15, 20, 30, 35, 40, 45	Spray region, steps of 1 mm

**Fig. 2.** Images of test cases with 0.8 s exposure time and identical aperture. The field-of-view of the inset has dimensions 220×170 mm 2 (width \times height).

Taylor's hypothesis was used to convert timescales into length scales. An estimation of the kinematic viscosity is required to compute the Taylor-scale Reynolds numbers. For case H_{II} , this was done by using $\langle X_{O_2} \rangle$ and $\langle T \rangle$ at the respective radial position as input parameters in detailed equilibrium chemistry calculations with Chemkin-Pro software [44].

As shown in Fig. 3, $\langle U_z \rangle$ profiles measured in the absence of a spray gradually increase from the fuel rod wall to a region with nearly constant velocity, hereafter referred to as 'coflow core'. For case A_{II} , the $\langle U_z \rangle$ profiles exhibit a different behavior in that $\langle U_z \rangle$ is significantly augmented close to the fuel rod wall. This increase is accompanied by a significant augmentation of $\langle U_r \rangle$ as well (see Table 3). This behavior is caused by the spray which accelerates the coflow in the near-wall region. The presence of the spray also induces a significant increase of the degree of anisotropy near

**Fig. 3.** Mean axial velocity $\langle U_z \rangle$ and turbulence intensity $u'_z/\langle U_z \rangle$ for case A_{II} at $z = 0$ mm.**Fig. 4.** Mean axial velocity $\langle U_z \rangle$ and turbulence intensity $u'_z/\langle U_z \rangle$ for case H_{II} at $z = 0$ mm.

the wall and a considerable decrease in the coflow core. Figure 4 shows that $\langle U_z \rangle$ profiles for case H_{II} exhibit a similar behavior, i.e. an acceleration of the coflow takes place in the wall region. In the wall region, the value of $u'_z/\langle U_z \rangle$ is significantly higher than in case A_{II} .

It is also observed for cases A_{II} and H_{II} that at the most outer parts of the coflow $u'_z/\langle U_z \rangle$ increases substantially. This evidence for a shear layer between the coflow and the laboratory air and it is of importance for case H_{II} . The laboratory air gradually mixes with the hot-diluted coflow changing the coflow inlet temperature and oxygen radial distribution. It will be shown in Section 4.5.2 that up to $z = 40$ mm, the coflow inlet profiles are preserved within the radial positions between $-40 < r < 40$ mm.

The $\langle X_{O_2} \rangle$ profiles in Fig. 5 show a symmetric and homogeneous coflow over a wide radial distance for case H_{II} . In the $\langle T \rangle$ profiles, $\langle T \rangle$ decreases towards the fuel rod wall due to the heat losses to the water-cooling system. In the near-wall region, asymmetries are seen on opposite side of the spray axis that exceed the inaccuracy of the CARS system (over 100 K at $r = 18$ mm). This is attributed to the different interaction of the premixed flames of the secondary burner close to the fuel rod wall. In addition, at the coflow annulus ($r = 80$ mm) a difference of 200 K is observed on

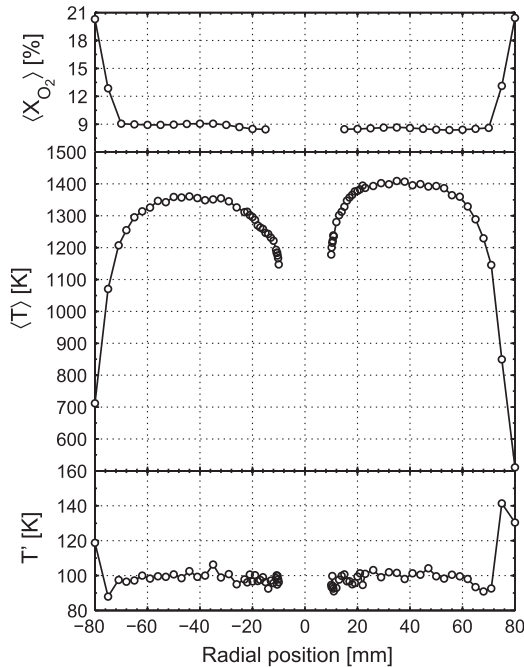


Fig. 5. Mean oxygen volume fraction $\langle X_{O_2} \rangle$, mean temperature $\langle T \rangle$ and root-mean-square temperature fluctuations T' profiles for case H_{II} at $z = 0$ mm.

opposite sides of the coflow. This results from a small offset of the vertical pipe relative to the fuel rod.

4.3. Liquid breakup mechanisms

High-speed visualizations of the liquid breakup were performed for cases NA_I , A_{II} and H_{II} . Six sequential images are displayed in 6 for case NA_I and in 7 for cases A_{II} and H_{II} . Exposure time and camera frame rate were adjusted to fully resolve the liquid disintegration and to produce an optimal optical contrast. For case NA_I , the field-of-view has size $8.5 \times 6.8 \text{ mm}^2$ and the frame rate was set to 40 kHz. The liquid breakup time scales for cases A_{II} and H_{II} differ from that of case NA_I . Therefore, the frame rate was increased to 120 kHz at the expense of reducing the field of view to $6.8 \times 3.0 \text{ mm}^2$. The resolution of the imaging system was $26.6 \mu\text{m}$ per pixel for all the cases. The original video for each one of the three cases are available in the [supplementary materials](#).

The Weber number for cases NA_I , A_{II} and H_{II} is 0.46, 3.26 and 0.46 respectively. For case H_{II} , a mean temperature gradient exists in the wall region, therefore, the thermophysical properties of the gas (needed to estimate the We number) were taken at $r = 11 \text{ mm}$ which are more representative of the conditions in the breakup region than those of the coflow bulk mean temperature.

Figure 6(a) ($t = 0 \text{ s}$) shows liquid emerging from the atomizer orifice in the form of a conical sheet. Liquid fuel passes through inclined tangential slots in the atomizer chamber inducing centrifugal forces

that cause the liquid flow to diverge radially. In the conical sheet, sinuous waves and short-wavelength surface disturbances are observed, each with different dynamics. Sinuous waves start near the orifice with low amplitude with respect to the wavelength. As the liquid sheet moves in the downstream direction 6(a-d), the amplitude of the sinuous waves grows and the distance between successive short-wavelength disturbance crests increases. The sinuous wave amplitude growth leads to a thinning of the local sheet thickness between successive crests and small perforations of the liquid sheet occurs. As a rule, the liquid sheet disruption occurs in the regions with minimal sheet thickness yielding toroidal structures, lobes and small droplets.

The resulting fragments proceed into further breakup to a point where the restoring surface tension overcomes the disruptive aerodynamic forces and the breakup process ceases (see 6(e and f)). Small perforations also occur in regions of the liquid sheet where no large wave amplitude are present. However, from the high-speed recordings, it is not clear whether such event results from the shear in the liquid–air interface or the liquid initial turbulence.

Similarly, for case A_{II} , small perforations occur in the conical sheet. These perforations rapidly evolve and yield toroidal structures that further disintegrate into droplets. However, the amplitude growth of sinuous waves at the liquid–air interface occurs faster than in the case NA_I and the onset of breakup occurs closer to the atomizer orifice. This is due to the higher Weber number. The larger aerodynamic interactions between the liquid sheet and the surrounding gas, enables the growth of the surface waves and the eventual disintegration of the sheet.

The breakup mechanism for case H_{II} differs from the previous cases. As the liquid emerges from the atomizer orifice (see 7a and b), no wave amplitude growth is evident and a 'lump' of liquid immediately disrupts from the main liquid conical sheet. We believe that vaporization contributes to the local thinning of the conical liquid sheet. As the sheet thickness rapidly decreases, any perturbation causes the thin sheet to tear resulting in liquid lumps that subsequently disintegrate into ligaments and droplets (7c and e). It is also evident that some ligaments shrink and depending on their initial size and geometry may either form a single droplet or breakup into smaller lobes and 'satellite' droplets.

4.4. Spray in air coflow structure – case A_{II}

4.4.1. Droplet diameter distribution and mean velocity field

Profiles of the Sauter mean diameter (d_{32}) at five axial distances, $z = 10, 20, 30, 40$ and 45 mm along with the mean gas and droplet velocity fields are presented in Fig. 8. At each axial station, radial transverses were performed in steps of 1 mm. The dashed line superimposed in the mean velocity field marks the locations where flame luminescence reaches a maximum. Hereafter, for case A_{II} , the 'center-region' refers to the region near the axis surrounded by the adjacent inner flame-front whereas the 'outer-region' refers to the most outer part of the spray beyond the outer flame-front.

Table 3

Summary of the relevant turbulence statistics in the coflow.

			w/o Spray	A_{II}	H_{II}
Radial position	R	[mm]	19	50	12
Axial velocity	$\langle U_z \rangle [\times 10^2]$	[m/s]	18.16	28.94	93.05
Radial velocity	$\langle U_r \rangle [\times 10^2]$	[m/s]	3.05	1.82	65.55
Axial turbulence intensity	$u'_z / \langle U_z \rangle$	[%]	18.16	2.68	2.30
Axial r.m.s. of fluctuations	$u'_z [\times 10^2]$	[m/s]	6.32	0.77	2.14
Radial r.m.s. of fluctuations	$u'_r [\times 10^2]$	[m/s]	4.60	0.81	1.92
Anisotropy	u'_z / u'_r	[-]	1.37	0.96	1.11
Taylor micro-scale	λ_g	[mm]	–	6.60	–
Taylor–Reynolds number	Re_λ	[-]	–	90	–

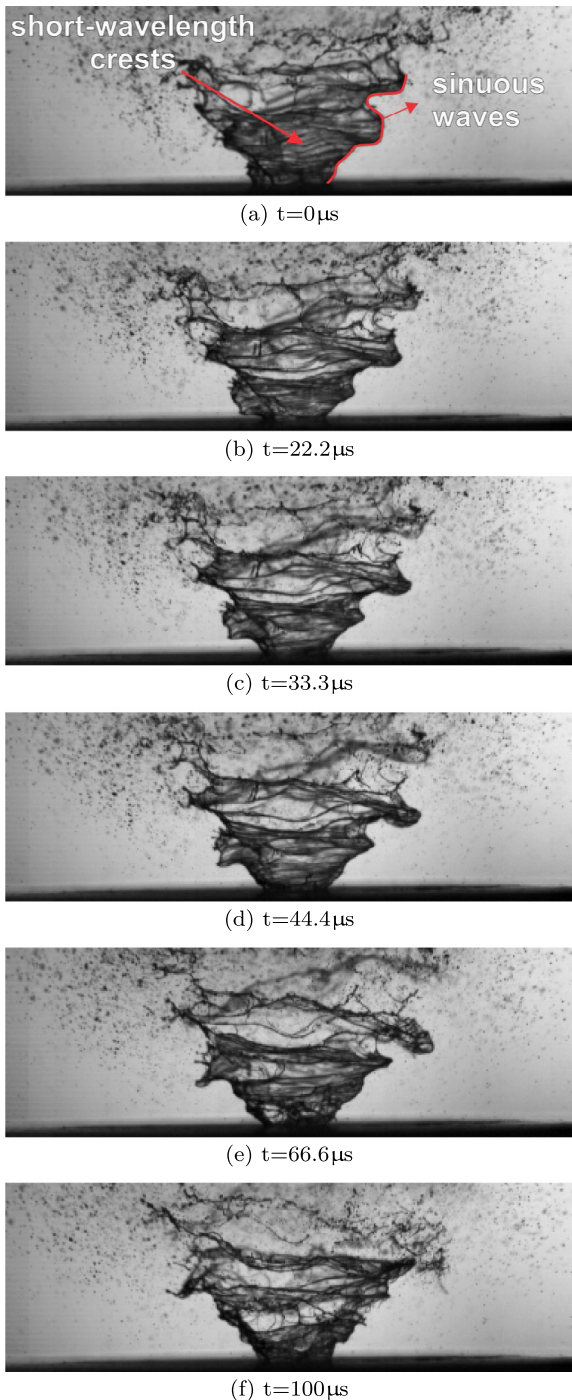


Fig. 6. Sequence of images showing the liquid sheet breakup for case NA₁ ($We = 0.46$). The field-of-view has dimensions $9.68 \times 3.04 \text{ mm}^2$.

At $z = 10 \text{ mm}$, the maximum difference between (d_{32}) values at corresponding points on opposite sides of the spray axis is $1.9 \mu\text{m}$. Small droplets are present in the center-region and move mainly upwards. At larger distances from the spray axis, droplets size and average radial velocity increase indicating that a spreading of the spray into the coflow occurs. The data are consistent with the expected inertial response time associated with the droplet size. The small droplets resulting from the liquid jet breakup are responsive to the turbulence gas field and, therefore, are convected to the center due to the mean inward convective motion of the coflow caused by the spray presence. Above $z = 20 \text{ mm}$ an abrupt

reduction of the (d_{32}) is observed in the region between the inner and outer flame-front as a consequence of the rapid evaporation of the droplets caused by the appreciable heat-release from the oxidation process. As observed in the mean gas flow field, a significant increase of gas-phase velocity takes place in this region as well. This supports the idea that oxidation occurs since the expansion of the combustion gases induces a local acceleration of the gas-phase. Large droplets are present at the outer-regions where no visible reactions are evident.

4.4.2. Gas-phase velocity, temperature and droplet number density

To study the influence of the droplets on the local turbulence structure and composition of the gas-phase, droplet number density n_d along with the gas-phase mean axial velocity $\langle U_z \rangle_g$ and mean temperature $\langle T \rangle$ radial profiles are plotted in Fig. 9 at four axial stations, $z = 10, 20, 30$ and 45 mm . No CARS measurements were performed at axial stations below the lift-off height since the system inaccuracy exceeds the expected gas-phase temperature variation due to droplet evaporative cooling. To represent the large amount of data, the physical properties are jointly shown. The differently colored y-axis scales are used for the aforementioned physical quantities and the corresponding ranges have been preserved over the four axial stations. Droplets with diameter below $4 \mu\text{m}$ from the full record were taken as gas tracers for locations below the lift-off height. At the other axial stations the droplet diameter threshold was set to $8 \mu\text{m}$. The results of the gas-phase are limited by the availability of the small droplets that fulfill the aforementioned constraints and each point presented in Fig. 9 is based on an ensemble of, at least, 100 samples. Figure 10 displays the radial distribution of the root-mean-square temperature fluctuations T' for three axial stations and complements the information given in Fig. 9.

At $z = 10 \text{ mm}$ droplets are mainly concentrated around $r = 6 \text{ mm}$. The $\langle U_z \rangle_g$ profiles resemble a uniform, top-hat profile. The corresponding $\langle U_r \rangle_g$ radial profiles (not shown) are nearly null in the center-region indicating that the gas-phase moves predominantly in the axial direction.

From $z = 10 \text{ mm}$ to $z = 20 \text{ mm}$, a decrease of $\langle U_z \rangle_g$ on the spray axis is accompanied by the spread of the $\langle U_z \rangle_g$ profiles as a consequence of the momentum flux from the spray center-region towards the periphery. Simultaneously, an increase of the droplet density occurs at larger radial distances from the axis. This results from the spreading of the droplets into the air coflow due to their initial droplet radial velocity component and relatively large Stokes number. CARS measurements were obtained even in the spray region with droplet density as high as 10^5 cm^{-3} . A sharp increase of the local gas temperature and corresponding r.m.s. fluctuations (see Fig. 10) are observed in two regions indicating the presence of: (1) an inner flame-front ($9 < r < 11 \text{ mm}$) that stabilizes inside the spray region and (2) an outer flame-front ($17 < r < 21 \text{ mm}$) sustained by the air entrained and the turbulent mixing with the fuel vapor from droplets at the outer-region.

With increasing axial distance, a gradual decrease of $\langle U_z \rangle_g$ along the burner axis is observed. In the region delimited by the inner and outer flame-front, it is observed that along with a substantial decrease of the droplet number density initially present at $z = 20 \text{ mm}$, $\langle T \rangle$ increases. This suggests that, as large droplets move across this region, fresh fuel vapor together reacts with the reminiscent oxygen in the mixture. Two observations can be made concerning the outer and inner flame-front: Firstly, the outer flame-front appears as a thin blue layer and moves farther away from the spray axis. This indicates that a lean mixture results from the mixing of fuel vapor with the air coflow at increasingly larger radial distances due to the spreading of the spray droplets. Secondly, the inner flame-front moves closer to the spray axis and a reduction of n_d takes place. It is hypothesized that the inner

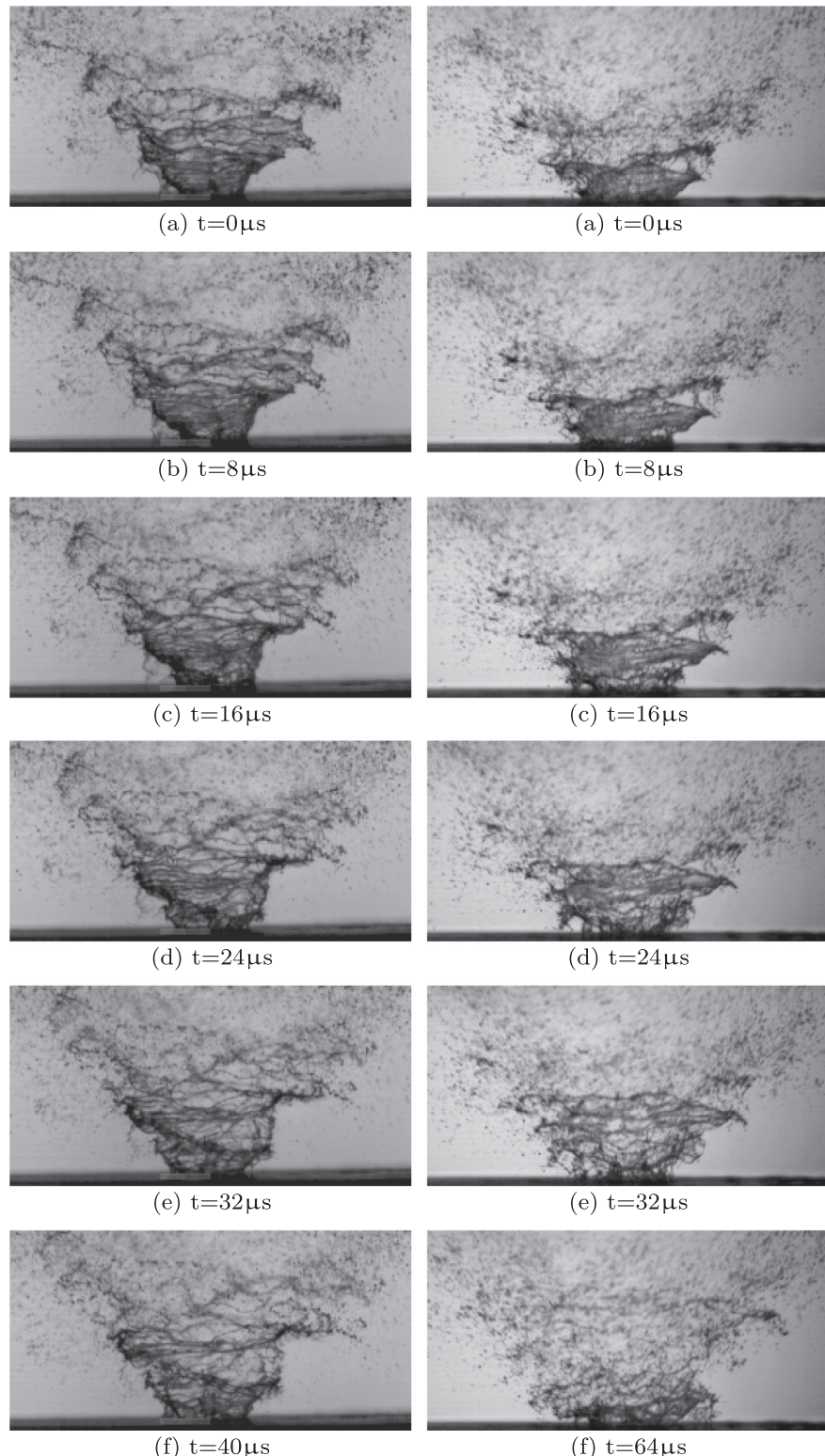


Fig. 7. Sequence of images showing the liquid sheet breakup for case A_{II} (left) and H_{II} (right) ($We = 3.26$ and 0.46 , respectively). Both cases have identical field-of-view dimensions, $6.81 \times 3.04 \text{ mm}^2$.

flame-front motion towards the center-region is related to the mechanism of flame propagation between droplets and the velocity at which it occurs is much influenced by the effective fuel-air ratio, i.e. droplet-vapor-air ratio [45–48]. Specifically, the combustion products formed in the region between the flame-fronts are transported by diffusion and convection towards the center-region.

The heat of the combustion products increase the local rate of supply of the fuel vapor that eventually mixes with the surrounding gas. Reaction subsequently takes place and the inner flame-front propagates towards the spray axis. However, droplets acts as heat sink and depending on the local number of droplets, inter-droplet distance and turbulence characteristics, the amount of heat-release

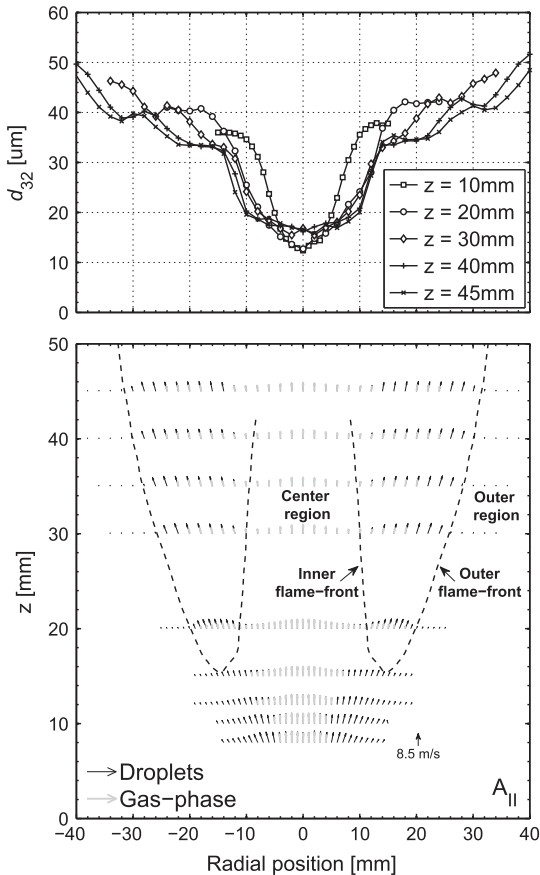


Fig. 8. Sauter mean diameter (d_{32}) profiles and mean gas and droplet velocity fields for case A_{II}. The dashed lines marks the maximum flame luminescence.

may not suffice to sustain the minimum temperature required to evaporate sufficient fuel vapor and, consequently, the flame propagation is halted.

4.4.3. Temperature histograms

Normalized temperature histograms for five radial positions at $z = 30$ mm are presented in Fig. 11 for case A_{II}. The total number of samples in each histogram amounts to 1000. A bin size of 50 K was selected for all the histograms presented. For each of the five radial positions selected, the corresponding mean $\langle T \rangle$, root-mean-square temperature fluctuation T' as well as skewness (S) and kurtosis (K) of the temperature distribution are presented in the table located on the top-left. Negative values of skewness indicate data that are skewed towards lower temperatures and that the left tail is long relative to the right tail. The high kurtosis values indicate that the distribution has a sharper peak and longer, fatter tails.

In the outer flame-front, $r = 22$ mm, the temperature distribution is rather broad with temperatures extending from 2400 K down to 1400 K. A considerable amount of samples are over 2000 K. For radial positions between the flame-fronts, i.e. $r = 20$ mm and $r = 16$ mm, $\langle T \rangle$ progressively decreases and the temperature distribution narrows significantly. At $r = 12$ mm a broadening of the observed temperature distribution along with a substantial number of samples over 2000 K is observed. In the inner flame-front, $r = 9$ mm, the number of peak temperatures increases as compared to $r = 12$ mm.

4.4.4. Droplet properties per size class

To illustrate the characteristics of the droplets behavior, the mean velocity $\langle U_z \rangle$ of four droplet size-classes at three axial stations, $z = 10, 20$ and 45 mm, are shown in Fig. 12. The class width

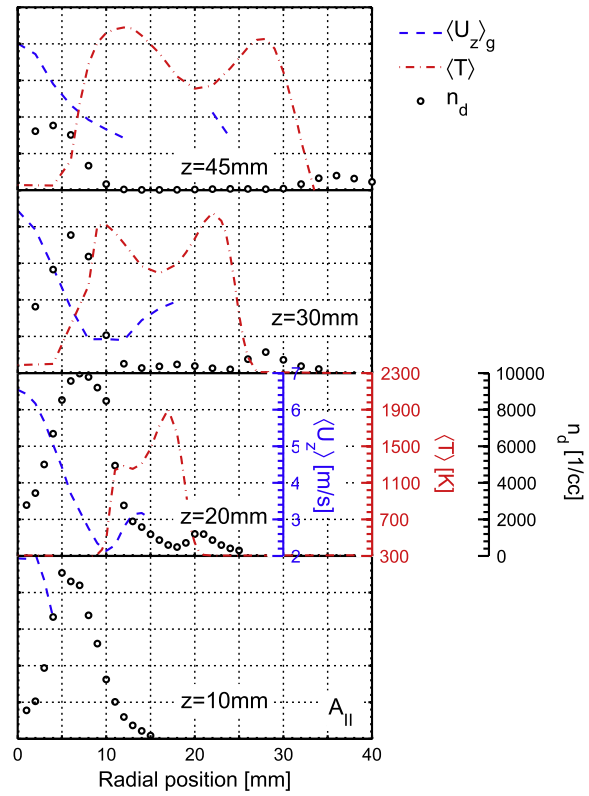


Fig. 9. Radial profiles of gas-phase mean axial velocity $\langle U_z \rangle_g$, mean temperature $\langle T \rangle$ and droplet number density n_d at four axial stations for case A_{II}.

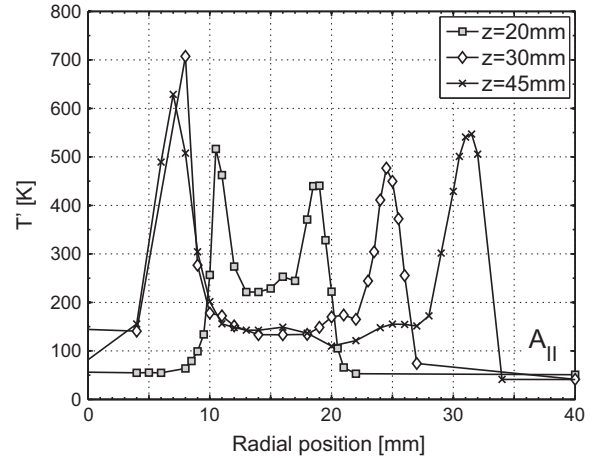


Fig. 10. Root-mean-square temperature fluctuations T' at $z = 20, 30$ and 45 mm for case A_{II}.

was chosen as $10 \mu\text{m}$. For the axial station below the lift-off height, $z = 10$ mm, droplets with diameter below $4 \mu\text{m}$ are considered flow tracers and the mean velocity representative of the gas-phase. For the remain axial stations, a threshold diameter of $8 \mu\text{m}$ was selected. All the points are an average of at least 200 samples. The difference between the mean velocity for a particular size class and the gas-phase mean velocity is called the slip velocity.

At $z = 10$ mm, it is observed that for larger droplets, the slip velocity relative to the gas-phase increases. This occurs as expected, since the Stokes number and, therefore, the respective inertial effects increase with the droplet diameter. Droplet $\langle U_z \rangle$ profiles present a distinct behavior depending on the droplet

diameter. Droplets smaller than $20\text{ }\mu\text{m}$, display an almost monotonic decrease of $\langle U_z \rangle$ with increasing radial distance from the spray center axis and the slip velocity is nearly zero in the center-region. For droplets larger than $30\text{ }\mu\text{m}$, $\langle U_z \rangle$ profiles show a single maximum at a radial position close to the center axis.

Three notable features can be observed on the droplet $\langle U_z \rangle$ profiles with increasing axial distance are as follows. First, in the center-region droplets smaller than $30\text{ }\mu\text{m}$ accommodate to the local gas-phase velocity. Secondly, droplets may 'survive' the region between both flame-fronts and eventually reach the air coflow, end up with nearly zero slip velocity and being carried upwards. Third, at the outer-region droplets smaller $30\text{ }\mu\text{m}$ tend to accelerate. The explanation is that due to the gas expansion and low initial droplet slip velocity, a reversal of the initial momentum flux, i.e. from the gas to the droplets, is established yielding an increase of those droplet size-class mean axial velocity.

4.5. Spray in hot-diluted coflow structure – case H_{II}

The following section concerns the results of flame H_{II} and they are presented in the same manner as flame A_{II} . The most notable features of flame A_{II} are recalled whenever appropriate so as to compare with the distinct peculiarities of flame H_{II} .

4.5.1. Droplet diameter distribution and mean velocity field

Profiles of (d_{32}) at five axial distances, $z = 10, 15, 20, 30$ and 40 mm along with the mean gas and droplet velocity fields are presented in Fig. 13 for case H_{II} . Flame luminescence is marked by the dashed line superimposed on the mean velocity fields. As in case A_{II} , an outer flame-front is visible and at the most outer parts of the spray, droplets are present in a region where no reaction is evident from the luminescence is observed. This region will be referred to as 'outer-region'. Droplets are virtually absent for locations above $z = 45\text{ mm}$ whereas in case H_{II} droplets are still present for higher axial stations.

The (d_{32}) distribution at $z = 10\text{ mm}$ qualitatively resembles that of case A_{II} . (d_{32}) is about $10\text{ }\mu\text{m}$ in the spray axis and increases for large radial distances from the spray axis. The maximum difference between (d_{32}) values at corresponding points on opposite sides of the spray axis is of $1.8\text{ }\mu\text{m}$. With increasing axial distance, droplets spread into the hot-diluted coflow and a substantial region in the center becomes void of droplets.

4.5.2. Gas-phase velocity, temperature and droplet number density

Figure 14 shows the gas-phase mean axial velocity $\langle U_z \rangle_g$ and the mean temperature $\langle T \rangle$ along with droplet number density n_d at

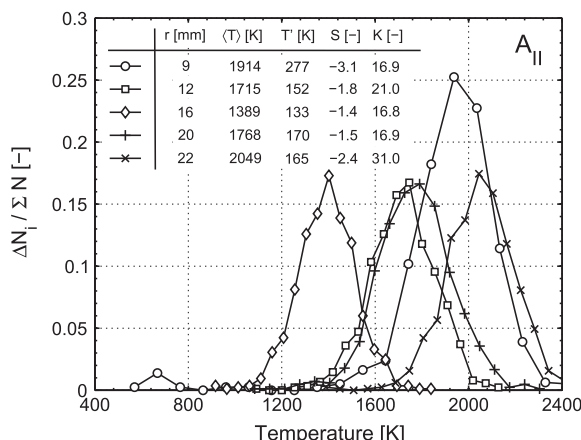


Fig. 11. Normalized temperature histograms across the spray outer-region at $z = 30\text{ mm}$ ($\Sigma N = 1000$ samples) for case A_{II} .

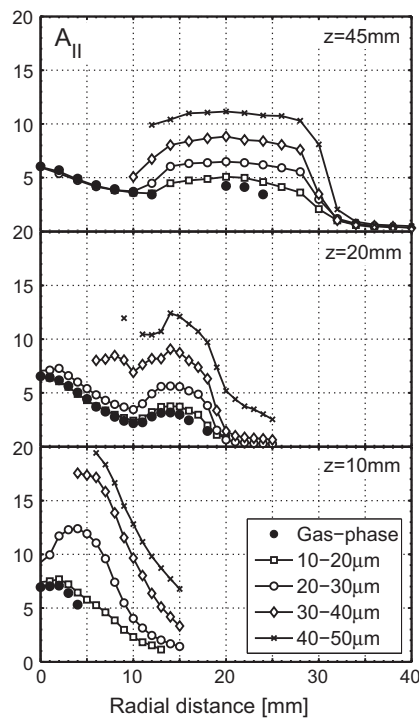


Fig. 12. Mean axial velocities $\langle U_z \rangle$ radial profiles per size class for case A_{II} .

four axial stations for case H_{II} . Due to the high droplet density in the region close to the spray nozzle, only a small number of valid CARS samples were acquired at $z = 10\text{ mm}$ and, therefore, no mean temperature profiles are presented for that axial station. Each of the different physical quantities is represented by a colored y -axis scale and the scale is the same for the four axial stations. Figure 15 displays the root-mean-square temperature fluctuations T' radial distribution at four axial stations and complements the information presented in Fig. 14.

In Fig. 14 it is observed that at $z = 10\text{ mm}$ droplets are mainly concentrated around $r = 7\text{ mm}$ and the n_d values are small as compared to those of case A_{II} . $\langle U_z \rangle_g$ profiles exhibit a 'dip' in the spray axis contrasting to what is observed in case A_{II} (see Fig. 9).

At $z = 15\text{ mm}$, the presence of droplets is evident at a larger distances from the spray axis. This indicates that the droplet motion bears resemblance to that of case A_{II} in that droplets spread into the coflow due to their initial outward radial momentum. A mean temperature difference of about 500 K is observed from the coflow core to a single peak located at $z = 15\text{ mm}$, $r = 13\text{ mm}$. $\langle T \rangle$ gradually decreases from the peak temperature towards the spray axis where the observed values are lower than that of the coflow, yet, significantly higher than the ethanol ignition temperature ($T_{ig} = 653\text{ K}$).

It is hypothesized that local temperature in the spray region depends much on the initial spatial distribution of the droplets. As the liquid fuel breaks up into droplets, the hot-diluted coflow is entrained towards the spray axis. The entrained coflow initially encounters an increasing number of droplets and, therefore, available surface area for heat and mass transfer. A significant amount of energy is needed to supply the liquid latent heat and vaporize the liquid droplets. Hence, the gas-phase temperature decreases from the coflow core to lower values at the spray axis. Likewise, the mixture fraction increases towards the center of the spray. Since the high oxygen dilution in the oxidizer stream causes a shift of the peak adiabatic temperature towards leaner mixtures, a flammable mixture is promptly formed at the outer-region. Furthermore, the hot-diluted coflow consists mostly of nitrogen, which is basically inert as far as the bulk chemical heat-release is

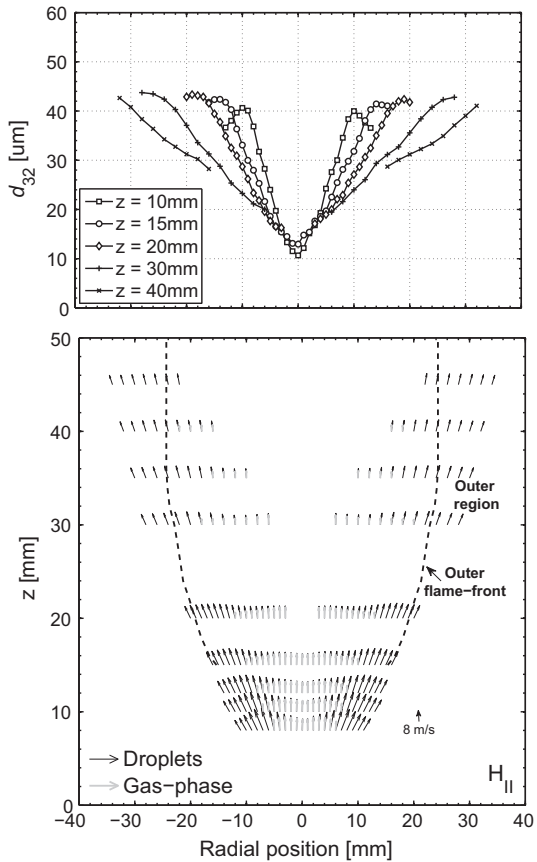


Fig. 13. Sauter mean diameter (d_{32}) profiles and mean gas and droplet velocity fields for case H_{II} . The dashed lines marks the maximum flame luminescence.

concerned, the combustion temperature and, hence, heat-release are reduced because of the expenditure of thermal energy to heat up nitrogen and other inerts. As a result, the temperature gradients observed at the outer flame-front are smaller than those of case A_{II} . Towards the spray axis, the amount of vapor diluted in the oxidizer becomes larger and the heat-release is gradually reduced yielding lower mean temperatures.

From $z = 15$ mm to $z = 30$ mm, a simultaneous process of droplet spreading and evaporation occurs yielding a progressive widening of the spray flame. This is evident from the observed evolution of the peak temperature location and the presence of droplets at larger distances from the center axis for more downstream axial stations. The combustion products formed at the outer flame-front are entrained towards the spray axis and dilute further the mixture near the spray axis.

Figure 15 reveals three additional features of case H_{II} . First, at $z = 30$ mm, a peculiarity in the mean and r.m.s. temperature fluctuations radial profiles is observed. Between $r = 0$ and 8 mm, T' increases to a local peak and decreases to smaller values until $r = 14$ mm. At $r = 8$ mm, a substantially increase of $\langle T \rangle$ is also observed (see Fig. 14). The radial profiles at $z = 40$ mm are shown to prove that this observation is a real physical effect and not mere experimental error. This indicates that, as in case A_{II} , an inner flame-front is also present. However, for case H_{II} , as the spray evolves downstream the heat-release is significantly suppressed and no appreciable $\langle T \rangle$ increase is observed at the inner flame-front location. Secondly, at $z = 30$ mm, in the outer flame-front region T' are only higher by 100 K over the temperature fluctuations of hot-diluted coflow core. However, T' remains about three times smaller than the values observed in the outer flame-front of case A_{II} at the

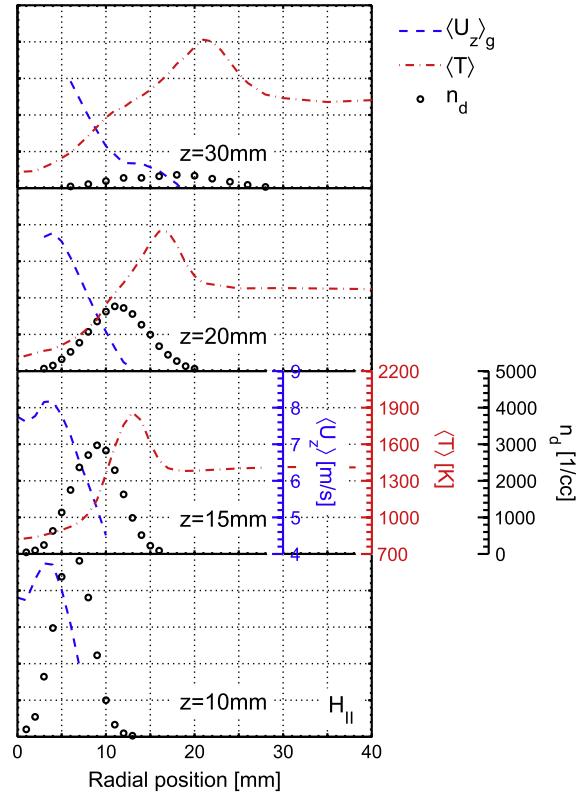


Fig. 14. Radial profiles of gas-phase mean axial velocity $\langle U_z \rangle_g$, mean temperature $\langle T \rangle$ and droplet number density n_d at four axial stations for case H_{II} .

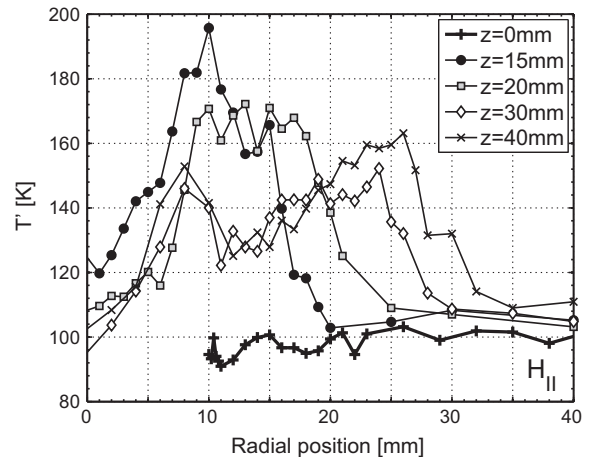


Fig. 15. Root-mean-square temperature fluctuations T' at $z = 0, 15, 20, 30$ and 40 mm for case H_{II} .

same axial location (see Fig. 10). Last, at $z = 30$ mm, the region of the outer flame-front ($14 < r < 27$ mm) is larger than the one of case A_{II} ($22 < r < 27$ mm) indicating that the characteristic flame thickness differs in both cases.

Figure 14 shows additional information concerning the influence of air entrainment on the coflow inlet temperature profiles. The laboratory air gradually mixes with the hot-diluted coflow changing the coflow initial radial temperature and oxygen distribution. It can be noticed that the coflow temperature at $r = 40$ mm remains nearly the same throughout the axial stations presented. This shows that, for the range of radial distances displayed, the burner pipe diameter is wide enough to isolate the

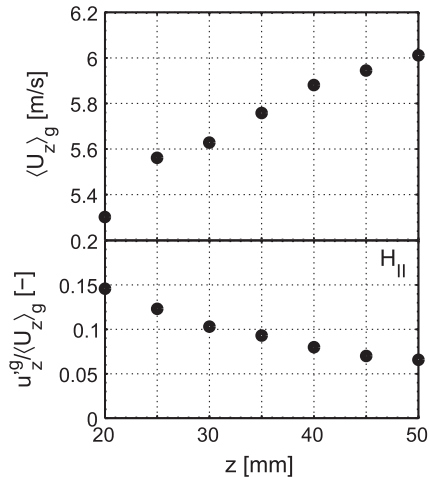


Fig. 16. Gas-phase mean axial velocity $\langle U_z \rangle_g$ and turbulent intensity $u_z^g/\langle U_z \rangle_g$ evolution along the spray axis for case H_{II} .

spray flame from the laboratory air entrainment. CARS measurements at higher axial stations (not shown) indicate that above $z = 60$ mm the outer region of the spray flame is perturbed by the laboratory air. Thus, below $z = 60$ mm, the spray flame is stabilized only by the hot-diluted coflow. Above the axial station of 60 mm, the oxidizer stream consists of a mixture of laboratory air together with hot-diluted coflow and reaction zone weakening effects may be present [49].

LDA measurements were carried out along the spray axis to better clarify the gas flow field. Gas-phase mean axial velocity $\langle U_z \rangle_g$ and turbulent intensity $u_z^g/\langle U_z \rangle_g$ are presented in Fig. 16. A LDA system can measure the velocities of both Al_2O_3 seeding particles that faithfully follow the gas-phase and of larger droplets, hence, 'cross-talk' from the velocity distribution of the droplets to that of the seeding particles results in significant velocity bias in the continuous phase statistics [50]. To avoid this, measurements were only carried out at axial positions above $z = 20$ mm, where no droplets are present.

An increase of $\langle U_z \rangle_g$ can be observed along with a gradual decrease of $u_z^g/\langle U_z \rangle_g$. At $z = 10$ mm, $\langle U_z \rangle_g$ profiles exhibit a 'dip' near the spray axis (see Fig. 14). These results show that the initial $\langle U_z \rangle_g$ gradients lead to turbulent diffusion of momentum in the center, yielding an enhancement of the axial momentum along the spray axis.

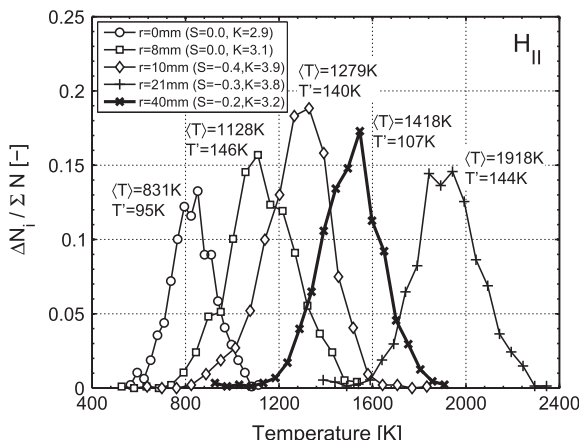


Fig. 17. Normalized temperature histograms for five radial positions at $z = 30$ mm ($\Sigma N = 1000$ samples).

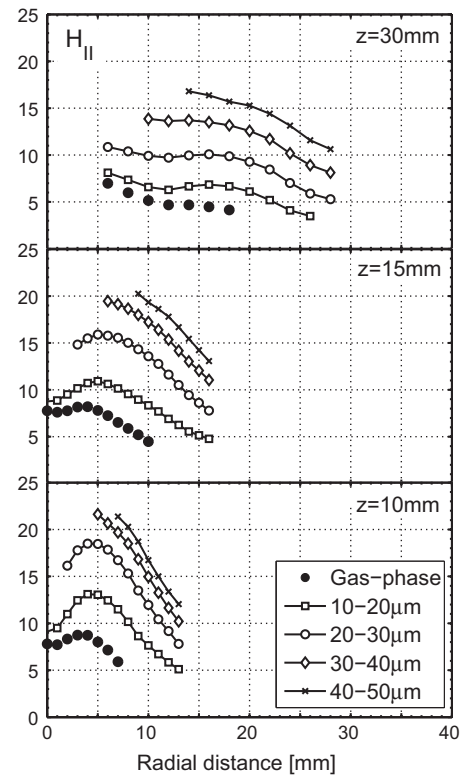


Fig. 18. Mean axial velocities $\langle U_z \rangle$ radial profiles per size class for case H_{II} .

4.5.3. Temperature histograms

The trend of the normalized temperature distribution from the coflow ($r = 40$ mm) towards the spray axis ($r = 0$ mm) at $z = 30$ mm are presented in Fig. 17. A bin size of 50 K was selected for all the histograms presented. Along with each histogram, the corresponding mean temperature $\langle T \rangle$ and r.m.s. temperature fluctuations T' is given. Skewness (S) and kurtosis (K) of the temperature distribution are presented in the legend on the top-left side.

At $r = 40$ mm, $\langle T \rangle$ and T' are 1421 K and 105 K, respectively. At the outer flame-front, $r = 21$ mm, T' is only about 50 K higher than that of the coflow and the normalized temperature histograms shape are rather alike, yet, shifted. It is also observed that the number of samples above $T = 2000$ K is reduced as compared to the ones observed in case A_{II} (see Fig. 11). For $r = 10, 8$ and 0 mm, $\langle T \rangle$ successively decreases and only minor changes on the normalized histograms are observed. It is evident that in the region of the inner flame-front, $r = 8$ and 10 mm, no peak temperatures above 2000 K are present. At $r = 0$ mm a substantial reduction of T' is observed and the temperature distribution is symmetric ($S = 0$). Temperature histograms along the spray axis above $z = 20$ mm (not shown) have virtually identical skewness value. This indicates that, as a result of the turbulent mixing, the gas-phase is rather homogeneous in the region of the spray axis.

4.5.4. Droplet properties per size class

Velocity profiles of selected size classes of droplet ensembles are presented in Fig. 18 for case H_{II} . The development of $\langle U_z \rangle$ for case H_{II} shows that, similar trends at $z = 10$ mm hold, i.e. increasing droplet slip velocity with the size-class is observed. A higher slip velocity of droplets between 10 and 20 μm is observed. Farther downstream, slip velocity gradually decreases and at $z = 30$ mm the different size-class radial profiles exhibit a similar mean axial velocity.

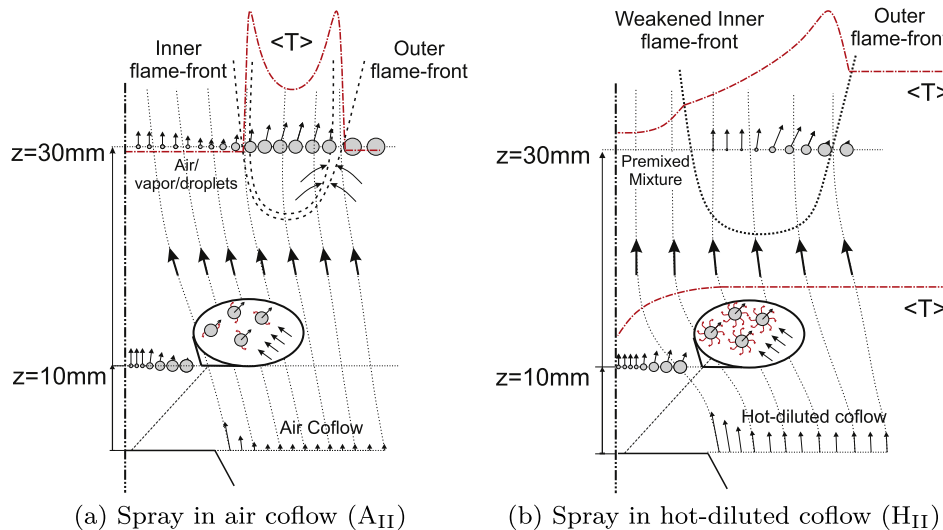


Fig. 19. Schematic of spray structure of pressure-swirl sprays in air and hot-diluted coflow. The dash-dotted line, represents the gas-phase mean temperature radial profile along the spray cross section.

5. Spray phenomenology in air and hot-diluted coflow

Figure 19 presents a schematic of the spray structure of A_{HII} and H_{HII} cases. The goal of this section is to provide a summary of the most notable features of both cases and elaborate a schematic illustration of the spray structure of both cases.

In the air coflow case, Fig. 19(a), the presence of the spray induces entrainment of the air coflow into the spray. As a result of the liquid breakup and the inward convective motion of the coflow generated by the spray, small droplets are mainly located in the center whereas large droplets are encountered at the most outer parts of the spray. While the large droplets spread into the air coflow and small droplets move upwards, the difference in velocity between gas and droplet enhance the droplets vaporization rate and fuel vapor is produced. An inner and an outer lean flame-front develops. The outer flame-front is sustained by the entrainment of air coflow and the fuel vapor from the large droplets at the most outer parts of the spray. The inner flame-front appears in a region inside the spray and gradually moves towards the center-region wherein a mixture of air and droplets and vapor fuel is present. It is hypothesized that this takes place through flame propagation mechanics and the speed at which it occurs depends on the local droplet-vapor-air mixture and gas turbulent characteristics. Furthermore, in the region between both flame-fronts, the fresh fuel vapor from the existing droplets and remaining oxygen in the combustion products may react further. Throughout most of the spray, a substantial number of temperature samples above 2000 K is observed.

In the hot-diluted coflow case, Fig. 19(b), the initial droplet (d_{32}) distribution resembles in many aspects that of the air coflow. The differences observed in the gas-phase velocity and temperature fields are due to the presence of strong vaporization rates which, consequently, yield a distinct turbulence modulation of the gaseous phase in the near atomizer region. As a result of the entrainment of hot-diluted coflow, droplets are embedded in a hot oxygen reduced gaseous phase and evaporate at the cost of heat losses from the gaseous phase. Hence, the temperature decreases towards the spray center. The temperature decrease is accompanied by an increase of fuel vapor towards the spray axis yielding a premixed region at the center. The significant oxygen dilution in the gaseous phase causes a shift of the stoichiometric mixture fraction towards leaner mixtures. Thus, the mixture formed at the most outer parts of the spray yields a broad outer flame-front with a single

temperature maximum. For the most inner parts of the spray, the mixture becomes increasingly rich yielding, therefore, progressively lower temperatures. Hence, a substantial reduction of temperature samples above 2000 K is observed and the temperature rise of the inner flame-front is substantially smaller as compared to the air coflow case.

6. Conclusion

6.1. Experimental results

A comprehensive study was performed of combusting ethanol sprays with similar injection pressure in air and hot-diluted coflow conditions. The objective was to describe the features of spray combustion in conventional and hot-diluted combustion regimes. The experimental investigations involved high-speed visualization of the liquid jet breakup and complementary pointwise measurement techniques in the spray region. Measurements of droplet size and velocity components in the spray region were obtained by PDA. CARS measurements were carried out in the spray region. The data processing procedure used to take into account the effects of the presence of droplets on the CARS spectra provides reliable and consistent gas-phase temperature measurements.

The experimental results show that the presence of strong vaporization rates produces significant changes of liquid breakup mechanics and of the gas-phase mean velocity in the near atomizer region. The coflow temperature and oxygen dilution have a profound impact on the spray flame structure and, ultimately, on the temperature peaks observed. In air coflow, droplets are embedded in air as gaseous phase. An inner and outer flame-front is observed. The inner flame-front propagates towards the small droplets embedded in an upward flow of air depending on the local vapor fuel-droplet distribution and flow conditions. In the hot-diluted coflow, the existence of a hot and diluted surrounding gaseous phase around the droplets instead of air has two effects: (1) a shift of the peak adiabatic temperature towards leaner mixtures and (2) enhancement of the droplets vaporization rates. The mixing of the droplet spray and the hot-diluted coflow, and the rapid evaporation together provide a radial gas composition profile with the gaseous mixture increasingly rich towards the spray center-region. This yields progressively lower temperatures towards the spray axis and a substantial reduction of peak temperatures.

6.2. Value for model validation

The experiments reported here provide a detailed dataset for model validation and new opportunities compared to other datasets reported in the literature [9]. The pressure-swirl atomizer leads to a spray with both dense-and dilute-regions. Model validation studies aiming at predicting the properties of the droplets usually collect information on the effects of the dense-region on the spray entering the dilute-region in one of two ways: (1) by a phenomenological model of spray breakup or (2) by the measured droplet and gas-phase statistical properties at the start of the dilute-region. The experimental database provides sufficient information to define the boundary conditions for both approaches. In the first approach, i.e. in case a liquid breakup model is adopted, the liquid fuel mass flow rate, injection pressure and temperature prior to the atomization is available. This information is complemented with the coflow velocity, temperature and composition profiles at the atomizer exit plane. Some other required input parameters (e.g. spray angle) can be estimated from the measured droplet density or the high-speed visualizations. The present work also provides the data needed for the second approach. Gas-phase axial and radial velocity and temperature statistics, respectively from LDA and CARS, together with droplet joint axial and radial velocity and size statistics from PDA, are available. However, this is not sufficient for a complete specification of the boundary conditions of the dilute-region. Due to the high slip velocity and the temperature differences between the liquid and the gas, evaporation starts well below the first measured axial station and a certain amount of fuel vapor is present at the start of the dilute-region. Thus, the profiles of fuel vapor at the boundary of the dilute-region must be provided by additional estimates.

The analysis of the experimental data has provided good evidence that air and hot-diluted coflow lead to changes in the local flame type and strength of heat-release. Those are difficult to predict by models using only a single type of local flame structure or only simple chemistry. Thus, the dataset offers the opportunity for testing models representing several possible types of local flame structure.

Acknowledgments

This work is financed by the Technology Foundation STW, Stork Technical Services and Shell. Bart Hoek and Erwin de Beus are kindly acknowledged for the technical support.

Appendix A. Supplementary material

Supplementary data associated with this article can be found, in the online version, at <http://dx.doi.org/10.1016/j.combust-flame.2014.07.033>.

References

- [1] J.A. Wünnigen, J.G. Wünnigen, *Prog. Energy Combust. Sci.* 23 (1997) 81–94.
- [2] A.S. Veríssimo, A.M.A. Rocha, M. Costa, *Fuel Process. Technol.* 106 (2013) 423–428.
- [3] M. Katsuki, T. Hasegawa, *Proc. Combust. Inst.* 27 (1998) 3135–3146.
- [4] A. Cavaliere, M. de Joannon, *Prog. Energy Combust.* 30 (4) (2004) 329–366.
- [5] B.B. Dally, A.N. Karpetis, R.S. Barlow, *Proc. Combust. Inst.* 29 (2002) 1147–1154.
- [6] M. Ihme, Y. See, *Proc. Combust. Inst.* 33 (1) (2011) 1309–1317.
- [7] E. Oldenhoef, M. Tummers, E. van Veen, D. Roekaerts, *Combust. Flame* 158 (8) (2011) 1553–1563.
- [8] E. Oldenhoef, M. Tummers, E. van Veen, D. Roekaerts, *Combust. Flame* 157 (2010) 1037–1234.
- [9] P. Jenny, D. Roekaerts, N. Beishuizen, *Prog. Energy Combust.* 38 (6) (2012) 846–887.
- [10] H. Tsuji, A.K. Gupta, T. Hasegawa, M. Katsuki, K. Kishimoto, M. Morita, *High Temperature Air Combustion: From Energy Conservation to Pollution Reduction*, first ed., CRC, 2002.
- [11] R. Weber, J.P. Smart, W. vd Kamp, *Proc. Combust. Inst.* 30 (2005) 2623–2629.
- [12] V.M. Reddy, D. Sawant, D. Trivedi, S. Kumar, *Proc. Combust. Inst.* 34 (2) (2013) 3319–3326.
- [13] V.M. Reddy, S. Kumar, *J. Propul. Power* 2 (2) (2013) 139–147.
- [14] B. Merci, D. Roekaerts, A. Sadiki (Eds.), *Experiments and Numerical Simulations of Diluted Spray Turbulent Combustion: Proceedings of the 1st International Workshop on Turbulent Spray Combustion*, ERCOFTAC Series, vol. 17, Springer, 2011.
- [15] G.M. Faeth, *Proc. Combust. Inst.* 26 (1996) 1593–1612.
- [16] A.N. Karpetis, A. Gomez, *Combust. Flame* 121 (1–2) (2000) 1–23.
- [17] W. O'Loughlin, A. Masri, *Combust. Flame* 158 (8) (2011) 1577–1590.
- [18] M. Derudi, R. Rota, *Proc. Combust. Inst.* 33 (2) (2011) 3325–3332.
- [19] V.G. McDonnel, M. Adachi, G.S. Samuelsen, *Combust. Sci. Technol.* 82 (1–6) (1992) 225–248.
- [20] V.G. McDonnel, G.S. Samuelsen, *J. Fluids Eng.* 117 (1995) 145–153.
- [21] J.F. Widmann, C. Presser, *Combust. Flame* 129 (1–2) (2002) 47–86.
- [22] I. Düwel, H.-W. Ge, H. Kronemayer, R. Dibble, E. Gutheil, C.E. Schulz, *Proc. Combust. Inst.* 31 (2007) 2247–2255.
- [23] W.P. Jones, S. Lyra, S. Navarro-Martinez, *Proc. Combust. Inst.* 33 (2) (2011) 2153–2160.
- [24] C. Heye, V. Raman, A.R. Masri, *Proc. Combust. Inst.* 34 (1) (2013) 1633–1641.
- [25] S. Ukai, A. Kronenburg, O.T. Stein, *Proc. Combust. Inst.* 34 (1) (2013) 1643–1650.
- [26] M. Linne, *Proc. Combust. Inst.* 39 (5) (2013) 403–440.
- [27] Y. Yue, C.F. Powell, R. Poola, J. Wang, J.K. Schaller, *Atomization Spray* 11 (4) (2001) 471–490.
- [28] J. Shinjo, A. Umemura, *Proc. Combust. Inst.* 33 (2) (2011) 2089–2097.
- [29] P. Medwell, B. Dally, *Combust. Flame* 159 (10) (2012) 3138–3145.
- [30] P.R. Medwell, Ph.D. thesis, University of Sydney, 2007.
- [31] G. Sarras, M. Stöllinger, D. Roekaerts, Transported PDF simulations of the Delft-jet-in-hot-coflow burner based on 3D FGM tabulated chemistry, in: THMT – 12. Proceedings of the Seventh International Symposium On Turbulence, Heat and Mass Transfer, Begell House Inc., Palermo, Italy, 2012, 10p.
- [32] H.E. Albrecht, N. Damaschke, M. Borys, C. Tropea, *Laser Doppler and Phase Doppler Measurement Techniques*, first ed., Springer, 2002.
- [33] L.H.J. Absil, Analysis of the Laser Doppler Measurement Technique for Application in Turbulent Flows, Ph.D. thesis, Delft University of Technology, 1995.
- [34] TSI, Phase Doppler Particle Analyzer (PDPA)/Laser Doppler Velocimeter (LDV) Operations Manual, 2005.
- [35] S.V. Sankar, W.D. Bachalo, *Appl. Opt.* 30 (12) (1991) 1487–1496.
- [36] P. Taylor, R. Dudek, D. Flaherty, T. Kaempfe, *J. Aerosol Sci.* 25 (2) (1994) 419–423.
- [37] J.A. Friedmann, M. Renksizbulut, *Combust. Flame* 117 (1999) 661–684.
- [38] E. van Veen, D. Roekaerts, *Appl. Opt.* 44 (32) (2005) 6995–7004.
- [39] E. van Veen, D. Roekaerts, *Combust. Sci. Technol.* 175 (10) (2003) 1893–1914.
- [40] D. Brüggemann, S. Heshe, *DACAPO-CARS Spectra Evaluation Code User's Guide*, Germany, 1993.
- [41] A. Cessou, D. Stepowski, *Combust. Sci. Technol.* 118 (4–6) (1996) 361–381.
- [42] D. Stepowski, P. Goix, A. Cessou, *Atomization Spray* 9 (1) (1999) 1–27.
- [43] M. Tummers, D. Passchier, *Meas. Sci. Technol.* 12 (10) (2001) 1641.
- [44] CHEMKIN-PRO 15112 Tutorials Manual, San Diego, California, 2011.
- [45] G. Myers, A. Lefebvre, *Combust. Flame* 66 (2) (1986) 193–210.
- [46] A. Neophytou, E. Mastorakos, *Combust. Flame* 156 (8) (2009) 1627–1640.
- [47] A. Umemura, S. Takamori, *Combust. Flame* 141 (4) (2005) 336–349.
- [48] A.P. Wandel, N. Chakraborty, E. Mastorakos, *Proc. Combust. Inst.* 32 (2) (2009) 2283–2290.
- [49] P. Medwell, R. Paul, P. Kalt, B. Dally, *Combust. Sci. Technol.* 181 (7) (2009) 937–953.
- [50] Y. Hardalupas, A. Taylor, *Exp. Fluids* 6 (2) (2004) 137–140.